

# Hollow porous $\text{FeF}_3 \cdot 0.33\text{H}_2\text{O}$ microspheres by $\text{AlPO}_4$ coating as a cathode material of Na-ion batteries

Min Liu, Xianyou Wang\*, Rui Zhang, Lei Liu, Hai Hu, Yu Wang, Shuangying Wei

National Base for International Science & Technology Cooperation, National-Local Joint Engineering Laboratory for Key Materials of New Energy Storage Battery, Hunan Province Key Laboratory of Electrochemical Energy Storage and Conversion, School of Chemistry, Xiangtan University, Xiangtan 411105, China

## ARTICLE INFO

### Keywords:

Sodium-ion batteries  
Cathode material  
Iron-based fluoride  
 $\text{AlPO}_4$  coating  
Electrochemical performance

## ABSTRACT

As the cathode material of Na-ion batteries based on conversion reaction, the iron-based fluorides have attracted ever-increasing attentions. Nevertheless, its poor electronic conductivity and side reactions usually lead to sluggish reaction kinetics and rapid capacity decay during cycling process, and thus limiting its practical application. Herein, a hollow porous  $\text{FeF}_3 \cdot 0.33\text{H}_2\text{O}$  microsphere is successfully prepared via a solvothermal route and further modified with  $\text{AlPO}_4$ . The results show that appropriate modification treatment can satisfactorily decrease charge-transfer resistance and enhance sodium diffusion rate. Compared with the pristine  $\text{FeF}_3 \cdot 0.33\text{H}_2\text{O}$ , 4 wt.%  $\text{AlPO}_4$ -coated sample shows a noticeable initial discharge capacity of  $290 \text{ mAh g}^{-1}$  in the range of 1.2–4.0 V, outstanding cycling stability ( $211 \text{ mAh g}^{-1}$  after 80 cycles) and excellent rate capability ( $167 \text{ mAh g}^{-1}$  at 2.0 C). The excellent electrochemical properties can be ascribed to the distinctively hierarchical mesoporous hollow structure of  $\text{FeF}_3 \cdot 0.33\text{H}_2\text{O}$ , which facilitates electrolyte permeation and rapid ionic as well as electronic transmission. Besides, the multifunctional  $\text{AlPO}_4$  modification layer can improve the electronic conductivity, suppress the surface side reaction and buffer the volume changes during cycling processes, thus boosting the enhancement of the electrochemical performance. Therefore, this study offers a new strategy for improving and modifying the electrochemical performances of cathode materials for sodium-ion batteries.

## 1. Introduction

Energy production and storage technology is increasingly concerned by all over the world. As the large-scale application of lithium-ion batteries (LIBs) in many fields, a number of defects (such as its lack of resources, high cost and safety problem, etc.) are gradually revealed, which thus prompts the exploration for sustainable alternatives to satisfy demands of energy storage [1,2]. Na-ion batteries (NIBs) have remerged as an ideal candidate for large-scale energy storage systems (ESSs), because of its low cost and natural abundance as well as the similar storage mechanism to LIBs [3,4]. However, since ion radius (0.102 nm) of  $\text{Na}^+$  is 34% larger than that (0.076 nm) of  $\text{Li}^+$ , and the ionization potential of Na is higher than that of Li, resulting in a lower energy and power density for NIBs [5]. Therefore, for the practical application of NIBs, exploring the new cathode materials with much higher capacity and power density as well as excellent electrochemical performance to meet the requirement of energy storage devices is urgently needed. In contrast to intercalation cathode materials like layered oxides, polyanionic compounds, pyrophosphates, and so on, the transition metal fluorides based on multi-electron conversion reactions

have attracted more and more interest owing to its great specific capacity and energy density [6–12]. Among all metal fluorides, iron-based fluorides are the most competitive and attractive alternatives owing to its high theoretical specific capacity, relatively bargain price and low toxicity [13–17].

Serving as a polymorph of iron-based fluoride, open framework  $\text{FeF}_3 \cdot 0.33\text{H}_2\text{O}$  possesses unique tunnel structure, which is greatly beneficial for improving  $\text{Na}^+$  storage performance and enhancing  $\text{Na}^+$  transport kinetics [18]. Nevertheless, in terms of practical application of iron-based fluoride as NIBs cathode material, it has been restricted due to its sluggish kinetics and low electronic conductivity resulted from the high ionicity of Fe-F bonds [19]. In addition, another limitation that affects the cycle and rate property of  $\text{FeF}_3 \cdot 0.33\text{H}_2\text{O}$  is large volume change during cycling process stemmed from the conversion reaction [20]. To overcome above obstacles, various efforts have been made, such as controlling the size of particles to shorten the transmission pathways of electrons and ions [21–28], doping with other metal cation ( $\text{Co}^{3+}$ ,  $\text{Cr}^{3+}$  or  $\text{Ti}^{4+}$ ) to decrease band gap [29–31], and mixing with conductive carbon-based materials (conductive carbon, acetylene black, graphene or carbon nanotubes) to increase electronic

\* Corresponding author.

E-mail address: [wxianyou@yahoo.com](mailto:wxianyou@yahoo.com) (X. Wang).

conductivity [32–38]. Although the electrochemical performance of the material, to a certain extent, has been improved by the above strategies, there are still plenty of shortcomings. For instance, since the carbon-based material as part of the cathode is electrochemically inert in NIBs, it will reduce the energy density of NIBs [39]. And doping with other metal cation still does not effectively restrict large volume changes. While another potential method to overcome the above barriers is the surface modification with ultrathin coating layer like MoS<sub>2</sub> [40], V<sub>2</sub>O<sub>5</sub> [41], and TiO<sub>2</sub> [42], which is an effective approach to enhance the electrochemical performance of materials. Lately, Cho et al. [43] has reported that, in contrast to other surface modification materials, coating with AlPO<sub>4</sub> can remarkably enhance the cycling performance of material through suppressing the structural changes and surface erosion.

AlPO<sub>4</sub> has the framework structures like zeolites and is used as catalysts or molecular sieves. Owing to lower cost, environmentally friendly as well as excellent electron and ion conductivities, it has also become a popular coating material in the cathode materials of LIBs [44,45]. Furthermore, the strong P–O bond and the high electronegativity of PO<sub>4</sub><sup>3−</sup> polyanions with Al<sup>3+</sup> can prevent side reactions by limiting direct contact of electrolyte as well as electrode. Therefore, it has been coated on a variety of cathode materials like BiF<sub>3</sub> [46], LiCoO<sub>2</sub> [47], Li[Li<sub>0.2</sub>Fe<sub>0.1</sub>Ni<sub>0.15</sub>Mn<sub>0.55</sub>]O<sub>2</sub> [44], et al. Nevertheless, to the best of our knowledge, it has rarely been reported for coating AlPO<sub>4</sub> on the surface of iron fluorides.

Herein, the hollow porous FeF<sub>3</sub>·0.33H<sub>2</sub>O microspheres fabricated through a solvothermal method are further coated with various amounts of AlPO<sub>4</sub>. The physicochemical and electrochemical performances of all the samples are systematically investigated by XRD, SEM, TEM, EDX, SAED, BET, XPS and electrochemical test. It has been found that 4 wt.% AlPO<sub>4</sub> coated FeF<sub>3</sub>·0.33H<sub>2</sub>O exhibits the optimal performance in contrast to other surface modification materials.

## 2. Experimental section

### 2.1. Material preparation

All chemicals were directly used without further purification. The hollow porous FeF<sub>3</sub>·0.33H<sub>2</sub>O was synthesized via a solvothermal approach. Firstly, 2.02 g iron nitrate nonahydrate (Fe(NO<sub>3</sub>)<sub>3</sub>·9H<sub>2</sub>O, Aldrich) was dissolved in 50 mL ethanol served as the solvent and agitated for 30 min. Then, 1 mL hydrogen fluoride (HF) (40 wt.%) was dropwise added into the above mixed solution accompanying by agitated stirring. After stirring for 60 min, the mixed solution was transferred to the steel autoclave, and further heated at 120 °C for 10 h. After cooling to room temperature naturally, the product was washed for six times with anhydrous ethanol to remove residual HF, then dried at 80 °C in vacuum atmosphere for 24 h.

To fabricate AlPO<sub>4</sub> modified FeF<sub>3</sub>·0.33H<sub>2</sub>O materials, 0.3 g Al(NO<sub>3</sub>)<sub>3</sub>·9H<sub>2</sub>O (Aldrich) and 0.1 g (NH<sub>4</sub>)<sub>2</sub>HPO<sub>4</sub> (Aldrich) were added respectively to anhydrous ethanol and deionized water under vigorous stirring, until both forming the uniform colorless solution. Then, a desired amount of as-prepared FeF<sub>3</sub>·0.33H<sub>2</sub>O powder was slowly dispersed into Al(NO<sub>3</sub>)<sub>3</sub> ethanol solution with stirring and followed by an ultrasound process for 30 min. Subsequently, (NH<sub>4</sub>)<sub>2</sub>HPO<sub>4</sub> solution was dropwise added into the above mixed solution under vigorous stirring. The weight ratio of AlPO<sub>4</sub> and FeF<sub>3</sub>·0.33H<sub>2</sub>O was 2:98. Samples of FeF<sub>3</sub>·0.33H<sub>2</sub>O modified with AlPO<sub>4</sub> were synthesized using different ratios of AlPO<sub>4</sub>:FeF<sub>3</sub>·0.33H<sub>2</sub>O (0, 2, 4 and 6 wt.%). Then, the resulting mixture was obtained by centrifugal separation, then dried in vacuum at 80 °C for 24 h. At last, the obtained product was transferred into a tube furnace to be calcinated in Ar gas at 230 °C in for 5 h and then cooled to obtain the FeF<sub>3</sub>·0.33H<sub>2</sub>O/AlPO<sub>4</sub> composites. The schematic diagram of the fabrication process for FeF<sub>3</sub>·0.33H<sub>2</sub>O/AlPO<sub>4</sub> cathode material was displayed in Scheme 1. In addition, the FeF<sub>3</sub>·0.33H<sub>2</sub>O with various AlPO<sub>4</sub> coating amounts of 0, 2, 4, and 6 wt.% were marked as

AF-0, AF-2, AF-4, and AF-6, respectively.

### 2.2. Material characterizations

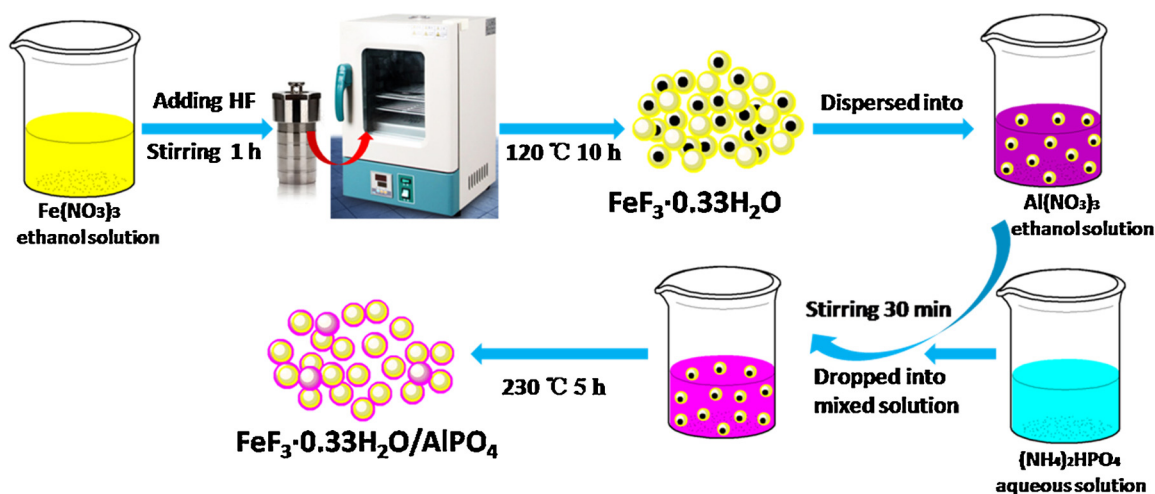
Crystal structures of materials were tested over the 2θ range of 10°–80° by Rigaku D/MAX-2500 X-ray diffraction (XRD) techniques with Cu-Kα radiation at a speed of 10° min<sup>−1</sup>. The morphologies of materials were determined via JEOL JSM-6610LV scanning electron microscope (SEM), Quanta FEG250 field emission scanning electron microscopy (FE-SEM) and JEOL JSM-2100F High-resolution transmission electron microscopy (HRTEM). The atomic concentration and elemental mappings of the materials were carried out by using a JEOL Quanta FEG250 energy-dispersive X-ray spectroscope (EDXS). The diffraction patterns were checked by employing the selected area electron diffraction (SAED, JEOL JSM-2100F) mode. The Brunauer–Emmett–Teller (BET) method was utilized to measure the specific surface area and pore size distribution of the samples via N<sub>2</sub> adsorption-desorption employing a BET instrument (Micromeritics TriStar II 3020, USA). The element analyses presenting in composites were investigated using K-Alpha 1063 X-ray photoelectron spectroscopy (XPS) with the Al Kα X-ray source. Before ex situ XRD or TEM test, the cycled electrodes were washed with dimethyl carbonate (DMC) to get rid of the residual sodium salt derived from electrolyte.

### 2.3. Electrochemical tests

The electrochemical properties of the FeF<sub>3</sub>·0.33H<sub>2</sub>O/AlPO<sub>4</sub> composites were tested in the CR2025 coin cells using metallic sodium as the counter and reference electrode. Active materials, acetylene black (EC) and polyvinylidene fluoride (PVDF) binder with a weight ratio of 8:1:1 in N-methyl-2-pyrrolidone (NMP), with aluminum foil current collector, were mixed to prepare the working electrodes. Glass microfiber filter from Whatman was utilized as the separator. The electrolyte employed involves a mixed solvent of 1 M NaClO<sub>4</sub> in diethyl carbonate (DEC), EC and propylene carbonate (PC) at a volume ratio of 1:1:1. The average loading mass of active material is approximately 1.5 mg cm<sup>−2</sup>. The cycling performances of the FeF<sub>3</sub>·0.33H<sub>2</sub>O/AlPO<sub>4</sub> electrodes were measured by charge-discharge tests at different current densities between 1.2 and 4.0 V on Neware battery tester (Shenzhen, China). Electrochemical impedance spectroscopy (EIS) and Cyclic voltammetry (CV) curves were obtained through an electrochemical workstation (VersaSTAT3, Princeton Applied Research). The frequency range of EIS was from 0.01 Hz to 100 kHz with the amplitudes of 5 mV. The CV tests were conducted at a scanning speed of 0.2 mV s<sup>−1</sup> between 1.2 and 4.0 V. All the tests were measured at room temperature.

## 3. Results and discussion

Fig. 1a depicts the XRD patterns of FeF<sub>3</sub>·0.33H<sub>2</sub>O/AlPO<sub>4</sub> composites. It can be clearly seen that all diffraction peaks are indexed to hexagonal tungsten bronze (HTB) structure FeF<sub>3</sub>·0.33H<sub>2</sub>O (PDF No. 76-1262) with a space group of Cmc<sub>2</sub>m, indicating the introduction of AlPO<sub>4</sub> and heat treatment at 230 °C will not cause the change of FeF<sub>3</sub>·0.33H<sub>2</sub>O crystal structure. The main peaks of all the samples are sharp, which indicate that the samples are well-crystallized. For the X-ray diffraction patterns of the coated samples, no any diffraction peaks corresponding to AlPO<sub>4</sub> have been observed, which is probably because the AlPO<sub>4</sub> coating layer on the surface of material is only a thin layer. To understanding the HTB structure FeF<sub>3</sub>·0.33H<sub>2</sub>O with unique tunnel, its crystal structure is shown in Fig. 1b. The FeF<sub>6</sub> octahedral chain is linked by the corner-sharing fluorine atom to form a huge hexagonal tunnel along the [001] direction, which is more beneficial for the transport and storage of Na<sup>+</sup>, compared with the traditional ReO<sub>3</sub> type FeF<sub>3</sub>. The local structures of water molecules in the tunnel act as a stabilizing frame skeleton, which is directly related to the migration path of Na<sup>+</sup> as well as insertion sites [48], while conductive AlPO<sub>4</sub>



Scheme 1. Schematic diagram of the fabrication process for  $\text{FeF}_3 \cdot 0.33\text{H}_2\text{O}/\text{AlPO}_4$  cathode materials.

coating layer can effectively increase the conductivity of  $\text{FeF}_3 \cdot 0.33\text{H}_2\text{O}$ .

The size and morphology of the pure  $\text{FeF}_3 \cdot 0.33\text{H}_2\text{O}$  and surface-modified materials are analyzed by SEM in Fig. 2. As being seen from Fig. 2a, the pristine  $\text{FeF}_3 \cdot 0.33\text{H}_2\text{O}$  presents approximately  $1 \mu\text{m}$  hollow microsphere morphology with uniform size. After coating  $\text{AlPO}_4$  in Fig. 2b–d, the basic morphology of  $\text{FeF}_3 \cdot 0.33\text{H}_2\text{O}$  is not evidently changed. Nevertheless, the original pores basically disappeared due to the penetration of amorphous  $\text{AlPO}_4$ , and the size of the microspheres increased slightly as the coating amount increased. To further distinguish the effect of  $\text{AlPO}_4$  coating layer on the appearance and morphology of  $\text{FeF}_3 \cdot 0.33\text{H}_2\text{O}$ , the bare  $\text{FeF}_3 \cdot 0.33\text{H}_2\text{O}$  (AF-0) and the modified sample with 4 wt.%  $\text{AlPO}_4$  coating (AF-4) are compared. It can be clearly observed that the hollow microsphere with hierarchical structure has the porous shell and inner void as shown in Fig. 2e–f. Moreover, the HRTEM images of AF-0 displayed in Fig. 2g–h reveal that the hollow microspheres are composed of primal nanoparticles with a size of about 10 nm, which can attribute to the mechanism of Ostwald ripening and crystal growth [28]. The hierarchical and hollow porous structure possesses two outstanding merits: on the one hand, the dense pores in shell facilitate electrolyte infiltration into the inside electrode and make closely contact with the inner and outer surface, which leads to a higher surface area and a shorter transport length for  $\text{Na}^+$ ; on the other hand, the hollow core can accommodate the volume changes and improve cycle stability during  $\text{Na}^+$  insertion/extraction [49,50]. Furthermore, from the HRTEM image in Fig. 2i, apparent interplanar spacings can be indexed as 0.64, 0.37 and 0.32 nm correspond to (110), (220) and (002) planes of  $\text{FeF}_3 \cdot 0.33\text{H}_2\text{O}$ , respectively. Meanwhile, the corresponding SAED pattern (inset of Fig. 2i) further verifies that the prepared product is  $\text{FeF}_3 \cdot 0.33\text{H}_2\text{O}$ . After coated  $\text{AlPO}_4$  thin layer, the

surface of  $\text{FeF}_3 \cdot 0.33\text{H}_2\text{O}$  becomes more homogeneous than the pristine since small size  $\text{AlPO}_4$  particles attached to the surface of porous microspheres. The FE-SEM images of AF-4 reveal that the pores or gaps of microsphere are mainly filled with  $\text{AlPO}_4$  showed in Fig. 2j–k. The TEM (Fig. 2l–m) and HRTEM (Fig. 2n) images further confirm that the surface of the pristine particle is covered with an amorphous  $\text{AlPO}_4$  coating layer of about 5 nm thickness, which will help to stabilize its structure, reduce side reaction and increase cycling stability [43,44]. As shown in Fig. 2n, in the central region of the particle marked by the red circle, there are still many small domains of amorphous phase, indicating that the amorphous phase was infiltrated into the inner shell of hollow microspheres. The double-layer coating on the shell inside and outside surface of hollow microsphere can significantly improve the electronic conductivity of material and decrease side reactions, thereby enhancing the electrochemical properties of batteries.

To further inquire into the element composition and its distribution of material, the AF-4 composite was detected by EDXS, and the results are shown in Fig. 2o. The molar ratio of Al, Fe and P is close to 1:29:1, which is in good agreement with the initial experimental data. The dense accumulation of Fe spots corresponds to the active material of  $\text{FeF}_3 \cdot 0.33\text{H}_2\text{O}$ . The elemental mapping of Al displays a similar intensity distribution to that of P, suggesting that Al and P distribute evenly in/on the  $\text{FeF}_3 \cdot 0.33\text{H}_2\text{O}$  particles without phase separation as well as significant element enrichment.

The nitrogen adsorption/desorption isotherm was employed to measure the BET surface areas and the porous structure of  $\text{FeF}_3 \cdot 0.33\text{H}_2\text{O}$  hollow microspheres, and the results are presented in Fig. 3a. According to the  $\text{N}_2$  adsorption/desorption isotherms and the corresponding Barrett–Joyner–Halenda plots (inset of Fig. 3a), the

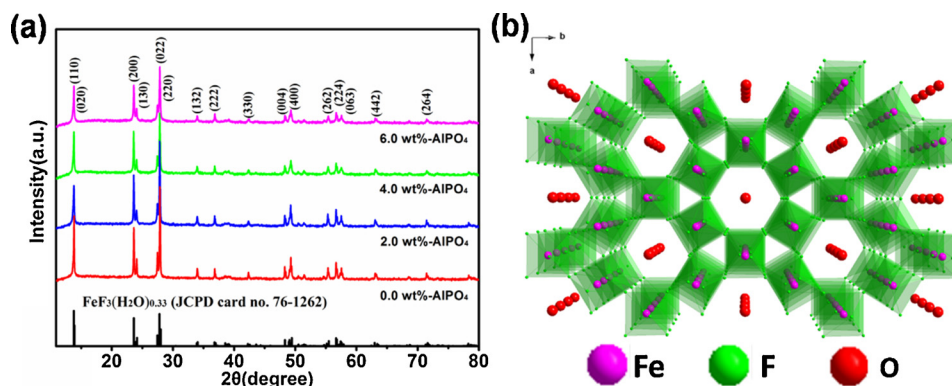


Fig. 1. (a) XRD patterns of the  $\text{FeF}_3 \cdot 0.33\text{H}_2\text{O}/\text{AlPO}_4$  composites. (b) Crystal structure of  $\text{FeF}_3 \cdot 0.33\text{H}_2\text{O}$ .

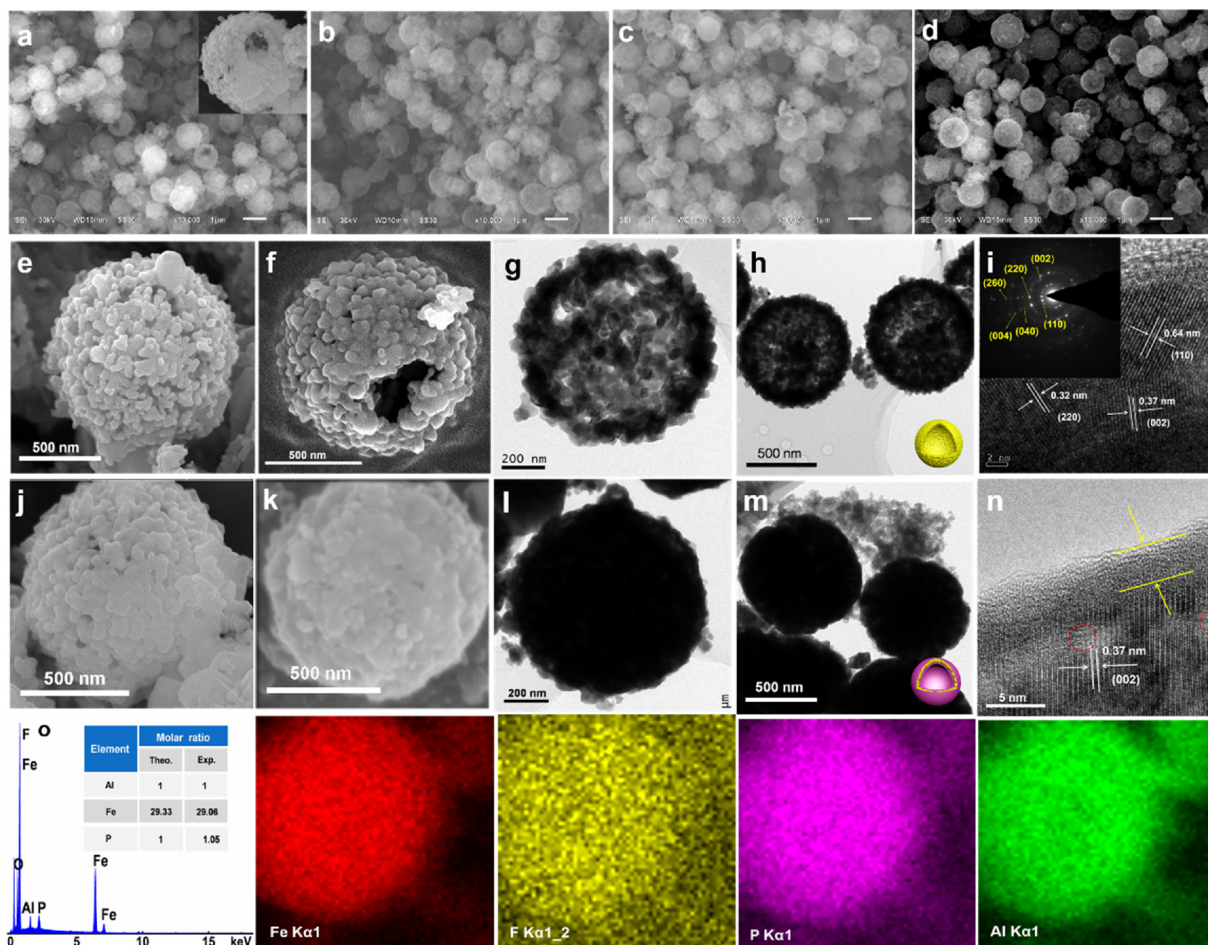


Fig. 2. SEM images of (a) AF-0, (b) AF-2, (c) AF-4 and (d) AF-6. (e–f) FE-SEM, (g–h) TEM and (i) HRTEM images of AF-0 sample; inset: the corresponding SAED pattern. (j–k) FE-SEM, (l–m) TEM and (n) HRTEM images of AF-4 sample. (o) EDX spectrum of (k) and corresponding EDX elemental distribution mapping; inset table exhibits the molar ratios of the Fe, Al and F elements.

specific surface areas and the average pore size of  $\text{FeF}_3 \cdot 0.33\text{H}_2\text{O}$  samples are approximately  $24.8 \text{ m}^2 \text{ g}^{-1}$  and 20 nm, respectively, which further confirms that the  $\text{FeF}_3 \cdot 0.33\text{H}_2\text{O}$  sample possesses porous structure characteristics. Meanwhile, in order to compare the influence of

$\text{AlPO}_4$  coating on the porous structure of the pristine, the BET specific surface area of AF-4 is calculated to be  $18.6 \text{ m}^2 \text{ g}^{-1}$  according to the nitrogen adsorption/desorption isotherm (Fig. 3b), and the corresponding average pore size of the AF-4 is about 12 nm (inset of Fig. 3b).

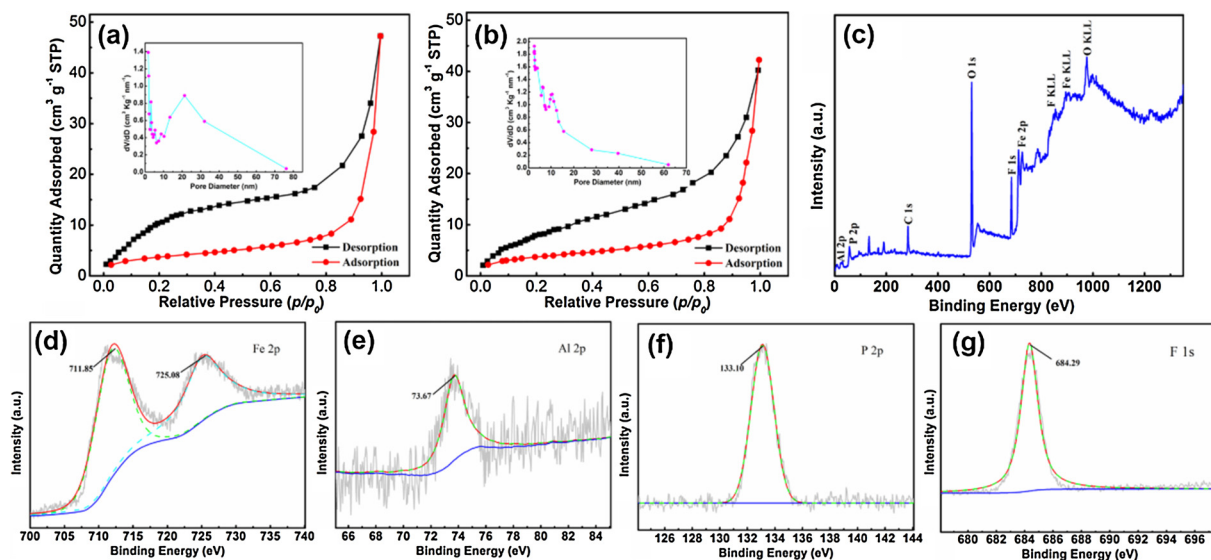
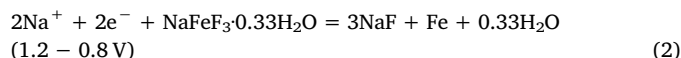


Fig. 3.  $\text{N}_2$  adsorption/desorption isotherms of (a) the pristine and (b) AF-4; inset: corresponding BJH pore size distribution plots. XPS spectra of AF-4: (c) the sum, (d) Al 2p, (e) Fe 2p, (f) P 2p and (g) F 1s.

Above results show that the sample coated with 4 wt.%  $\text{AlPO}_4$  still possesses a hollow porous structure, which can both accommodate the volume variation and facilitate electrolyte penetration and rapid ionic as well as electronic transmission during charge/discharge processes, thus resulting in the enhanced electrochemical performances [28].

XPS was used to verify the chemical composition and valence state of element. As being seen from the XPS spectrum of the AF-4 sample shown in Fig. 3c, the photoemission peaks of Fe, Al, P, F and O emerge. Fig. 3d exhibits the Fe 2p high resolution XPS spectrum, where the binding energy peaks position at 711.3 and 725.07 eV, which should be respectively attributed to Fe 2p<sub>3/2</sub> and Fe 2p<sub>1/2</sub> of the +3-oxidation state of iron [51,52]. The XPS spectrum of Al 2p exhibits a lower binding energy peak at 74.5 eV in Fig. 3e, which corresponds to  $\text{Al}^{3+}$  in  $\text{AlPO}_4$  compounds and is consistent with the date of the Al 2p<sub>3/2</sub> in the  $\text{AlPO}_4$  thin film [53]. In Fig. 3f, the binding energy of 134.1 eV is assigned to P 2p peak of  $\text{PO}_4^{3-}$ , which is a good match with the previous reported value of  $\text{AlPO}_4$  [54]. Therefore, the researches of Al 2p and P 2p spectrum verify further the existence of  $\text{AlPO}_4$  phase on the surface of  $\text{FeF}_3 \cdot 0.33\text{H}_2\text{O}$ . Furthermore, the binding energy of F 1s is centered at about 685 eV (Fig. 3g), which well corresponds to the Fe-F bonding [18].

To explore the mechanisms of storing Na ions, cyclic voltammogram (CV) experiments are carried out between 1.2 and 4.0 V. Fig. 4a presents the CV curves of AF-0 and AF-4 at a scan rate of  $0.2 \text{ mV s}^{-1}$ . The oxidation and reduction peaks stand for the sodium extraction and insertion processes, respectively. Meanwhile, the larger peak area in the CV usually corresponds to the higher capacity of the sample, and thus AF-4 provides a larger capacity compared to AF-0. It can be clearly seen that the CV profile of AF-0 shows one apparent reduction peak positioned at 2.0 V, corresponding to the intercalation of  $\text{Na}^+$  into  $\text{FeF}_3 \cdot 0.33\text{H}_2\text{O}$  crystal structures in Eq. (1). As the cathode material of sodium ion battery, Li et al. considered that during the discharging process, the electrochemical reaction involved at least two different reaction processes: intercalation in the high-voltage region of 1.2–4.0 V and a conversion reaction in the low-voltage region of 0.8–1.2 V [16,18]. The mechanism of  $\text{Na}^+$  storage of  $\text{FeF}_3 \cdot 0.33\text{H}_2\text{O}$  can be reflected as follows [35,55,56]:



Besides, the oxidation peak detected at 2.8 V can be seen. Based on the CV curve of AF-4 sample, it can be observed that redox peaks are generally in accord with that of AF-0. Nevertheless, the reduction peak appeared at 2.2 V and oxidation peak located at 2.7 V both have a small shift relative to that of AF-0, which implies the potential interval ( $\Delta E_p$ ) of the redox peaks of AF-4 is much smaller than that of AF-0, suggesting that AF-4 has a smaller electrochemical polarization as well as a superior cycle stability. Apparently, the enhanced cycle performance benefits from the introduction of the  $\text{AlPO}_4$  protective layer in the sample.

The electrochemical properties of the pristine and  $\text{AlPO}_4$ -coated  $\text{FeF}_3 \cdot 0.33\text{H}_2\text{O}$  are further investigated between 1.2 and 4.0 V by galvanotactic charge/discharge tests. Fig. 4b shows the initial discharge/charge curves of all samples at 0.1 C, where the distinct voltage hysteresis during the initial cycle could be related to reaction overpotential and diverse spatial distributions of electrochemically active phases [57]. There are few distinctions for the voltage plateaus of the AF-2, AF-4 and AF-6 with that of AF-0, illustrating that the  $\text{AlPO}_4$  modification has little effect on electrochemical behaviors of  $\text{FeF}_3 \cdot 0.33\text{H}_2\text{O}$ . For the curves of the AF-0, one voltage plateau appeared at about 2.3 V during the discharge process, which can be associated with the  $\text{Na}^+$  intercalation into  $\text{FeF}_3 \cdot 0.33\text{H}_2\text{O}$  structure. Additionally, the sample AF-4 displays the highest discharge voltage plateau and lowest charge voltage plateau, suggesting the smallest electrochemical polarization and outstanding reversibility, which consists with the results based on CV shown in Fig. 4a.

To study the impact of coating layer on the electrochemical behaviors of  $\text{FeF}_3 \cdot 0.33\text{H}_2\text{O}$ , the cycling performances of the pristine and  $\text{AlPO}_4$ -coated  $\text{FeF}_3 \cdot 0.33\text{H}_2\text{O}$  as the cathode for NIBs are tested at the current density of 0.1 C ( $1 \text{ C} = 200 \text{ mAh g}^{-1}$ ) between 1.2 and 4.0 V, as displayed in Fig. 4c. The first charge and discharge capacities of AF-0 are 267 and  $225 \text{ mAh g}^{-1}$  respectively, and the initial coulombic efficiency is only 84.26%; while AF-4 exhibits the initial discharge capacities of  $290 \text{ mAh g}^{-1}$  with a coulombic efficiency of 91.39%. The enhanced coulombic efficiency of the  $\text{AlPO}_4$ -modified sample can be ascribed to the fact which the  $\text{AlPO}_4$  coated layer can effectively lower

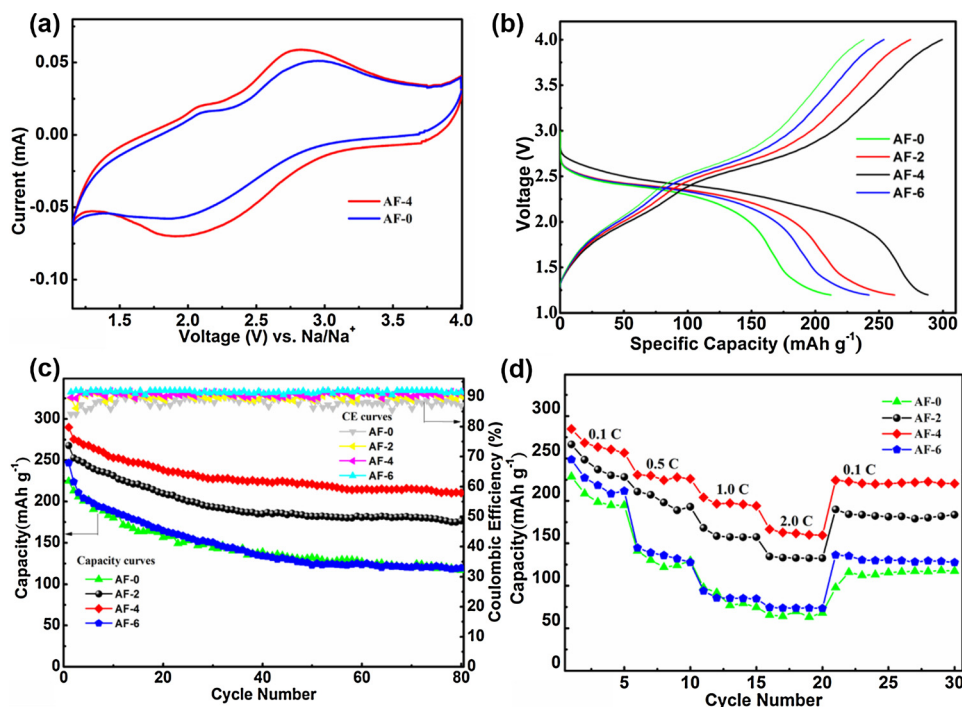


Fig. 4. (a) CV curve of AF-0 and AF-4 at a scan rate of  $0.2 \text{ mV s}^{-1}$  between 1.2 and 4.0 V. (b) Initial discharge and charge diagrams of all electrodes. (c) Cycling performances of all the electrodes at 0.1 C. (d) Rate capability of all samples varying rates from 0.1 to 2.0 C. At 0.1 C, between 1.2 and 4.0 V, (e) the cycling performances and (f) the initial discharge profiles of all electrodes.

the side reactions between electrolyte and electrode and prevent undesirable solid electrolyte interphase (SEI) from forming to some extent [23,39]. After 80th cycles, AF-0 can merely deliver the reversible capacity of  $117 \text{ mAh g}^{-1}$ , while AF-4 sample displays the highest discharge capacities of  $211 \text{ mAh g}^{-1}$ , which indicates that the cycleability and reversible capacity are enhanced considerably. The cycling performances of  $\text{FeF}_3 \cdot 0.33\text{H}_2\text{O}$  coated with 4 wt.%  $\text{AlPO}_4$  (AF-4) is obviously superior to that of the previously reported other iron fluoride cathodes in NIBs [13,15,16,18,32]. In addition, it is worth nothing that the AF-6 sample only maintains  $119 \text{ mAh g}^{-1}$  after 80 cycles, being lower than that of the AF-2 and AF-4, which is related to an unduly thick protective layer that may impede the transport of electrons and  $\text{Na}^+$ , leading to poor electrochemical performances and increasing the mass of the inactive material. Therefore, the above results suggest that appropriate  $\text{AlPO}_4$  modification (AF-4) may be beneficial to improve conductivities and increase discharge capacities of  $\text{FeF}_3 \cdot 0.33\text{H}_2\text{O}$ , while deficient (AF-0 and AF-2) or excess  $\text{AlPO}_4$  modification (AF-6) fail to improve electrochemical performances.

The rate performances of all the electrodes at various current densities (0.1–2.0 C) are shown in Fig. 4d. AF-2 and AF-4 samples exhibit better rate performance than that of AF-0 and AF-6, especially AF-4 presents the best rate property with discharge capacities of 285, 230, 204 and  $167 \text{ mAh g}^{-1}$  when the current density increase from 0.1 to 2.0 C. After the current densities return to 0.1 C, the corresponding capacity of AF-4 can keep  $220 \text{ mAh g}^{-1}$ , which is far over that of AF-0 of  $117 \text{ mAh g}^{-1}$ . Similarly, above results indicate that the rate performances of samples are remarkably improved by introducing  $\text{AlPO}_4$  protective layer with suitable thickness.

To explore electrochemical kinetics of sample, EIS measurements are carried out on all electrodes operated for 5 cycles. The EIS profiles of all samples as well as the corresponding equivalent circuit for fitting are presented in Fig. 5a. It can be observed that the EIS pattern of four samples possess the similar features and consist of one high-frequency semicircle as well as an inclined line at low-frequency region. The semicircle is related to the charge transfer resistance ( $R_{ct}$ ), reflecting the charge transfer kinetics. And the sloping line represents the Warburg resistance ( $Z_w$ ) of  $\text{Na}^+$  diffusion into the active material. In the equivalent circuit model, the electrolyte impedance ( $R_s$ ) corresponds to the total resistance of the electrolyte and electrode material. As we all know, the smaller radius of high-frequency semicircle demonstrates the lower value of  $R_{ct}$ . Obviously, AF-4 electrode has the smallest semicircle diameter contrast to that of AF-0, AF-2 and AF-6 after the 5th cycle, thus it has the lowest  $R_{ct}$ . These phenomenon is probably because the application of the  $\text{AlPO}_4$  protective layer is beneficial to transport of electrons, the increase of material conductivity and the diminution of the charge transfer resistance. Furthermore, the inclined lines of AF-2 and AF-4 are steeper than that of AF-0, which indicates that the  $\text{AlPO}_4$  coating layer is in favor of the transport of  $\text{Na}^+$ . The

semicircle diameter of AF-6 is bigger than that of AF-4, whereas the inclined lines of AF-6 is flatter compared with that of AF-0, which reveals that too thick protective layer not only enhances the charge transfer resistance but also hinders sodium ions diffusion, resulting in poor electrochemical performances.

The sodium ions diffusion coefficient ( $D_{\text{Na}^+}$ ), one of the key parameters as electrode active material of NIBs, revealed the tendency to be inversely proportional to the  $R_{ct}$ . The  $D_{\text{Na}^+}$  can be obtained by the following equation [58]:

$$D_{\text{Na}^+} = \frac{R^2 T^2}{2A^2 n^4 F^4 C^2 \sigma^2} \quad (3)$$

$$C = \frac{n}{V} = \frac{m/M}{V} = \frac{\rho V/M}{V} = \frac{\rho}{M} \quad (4)$$

Where  $R$  is the ideal gas constant,  $A$  is the surface area of electrode,  $T$  is the absolute temperature,  $F$  is Faraday's constant,  $n$  is the number of electron,  $C$  is the molar concentration of  $\text{Na}^+$  and can be calculated from Eq. (3).  $m$  is the mass of the material,  $M$  is the molecular mass and  $\rho$  is the density of the materials.  $\sigma$  is the Warburg impedance coefficient related to  $Z'$ :

$$Z' = R_s + R_{ct} + \sigma \omega^{-1/2} \quad (5)$$

Where  $\omega$  is the angular frequency. The linear relationships between  $Z'$  and  $\omega^{-1/2}$  of all the electrodes in the low frequency are exhibited in Fig. 5b. As can be known from calculation, the  $\text{Na}^+$  diffusion coefficient of AF-0 after the 5th cycle is  $3.34 \times 10^{-20} \text{ cm}^2 \text{ s}^{-1}$  (Table 1), which demonstrates that the AF-0 possesses a relatively lower diffusivity, probably due to structural changes and serious polarization. However, the corresponding  $\text{Na}^+$  diffusion coefficient of AF-4 after the 5th cycle is  $9.05 \times 10^{-19} \text{ cm}^2 \text{ s}^{-1}$ . Apparently, the  $\text{Na}^+$  diffusion coefficient of AF-4 is obviously higher than one of the AF-0. Therefore, above results indicate further that appropriate thickness  $\text{AlPO}_4$  protective layer can effectively promote the insertion/deintercalation process of  $\text{Na}^+$  and improve Na storage kinetics, thus enhancing its electrochemical properties.

Generally, the convective mechanism of  $\text{AlPO}_4$ -modified  $\text{FeF}_3 \cdot 0.33\text{H}_2\text{O}$  can be inferred as following. The unobstructed insertion/extraction in NIBs is closely related to the transmission speed of both electrons and sodium ions between electrolyte and active materials. For the pristine  $\text{FeF}_3 \cdot 0.33\text{H}_2\text{O}$  in Fig. 6a, the active materials are encircled by  $\text{Na}^+$  from electrolyte, thus guaranteeing the formation of “ $\text{Na}^+$ -bridge” around them. However, due to the low conductivity of  $\text{FeF}_3 \cdot 0.33\text{H}_2\text{O}$ , only partial regions of the surface of the  $\text{FeF}_3 \cdot 0.33\text{H}_2\text{O}$  are linked with electron through the material interface, which results in a low discharge specific capacity, low coulombic efficiency and poor electrode process kinetics. In terms of  $\text{AlPO}_4$ -modified  $\text{FeF}_3 \cdot 0.33\text{H}_2\text{O}$  cathode shown in Fig. 6b, the  $\text{AlPO}_4$  coating layer is evenly dispersed

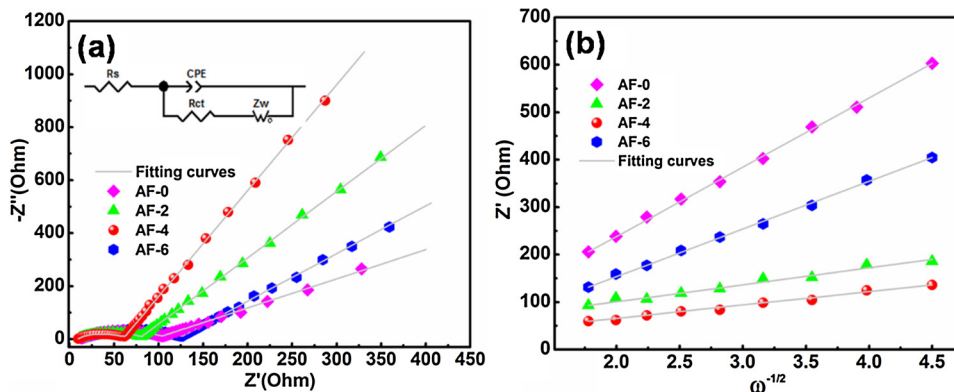


Fig. 5. (a) Nyquist plots of all the electrodes after the 5th cycle at 0.1C; inset: the corresponding equivalent circuit model. (b) The  $Z'$  vs.  $\omega^{-1/2}$  plots in the low-frequency region.

**Table 1**  
 $R_s$  and  $R_{ct}$  values of all the electrodes after the 5<sup>th</sup> cycle.

Samples	AF-0	AF-2	AF-4	AF-6
$R_s$ ( $\Omega$ )	13.02	11.47	9.70	16.91
$R_{ct}$ ( $\Omega$ )	104.61	81.86	61.36	126.47
$D_{Na^+}$ ( $\text{cm}^2 \text{s}^{-1}$ )	$3.34 \times 10^{-20}$	$5.59 \times 10^{-19}$	$9.05 \times 10^{-19}$	$7.06 \times 10^{-20}$

on the  $\text{FeF}_3 \cdot 0.33\text{H}_2\text{O}$  surface, constructing an immaculate “e-bridge” linking solid/liquid interface and a good conductive net. Since appropriate amount of  $\text{AlPO}_4$ -modified layer cannot densely adhere to active material, there are still reliable “ $\text{Na}^+$  bridges” retained for  $\text{Na}^+$  diffusion. Above “ $\text{Na}^+$ -bridge” and “e-bridge” provide more active sites for intercalation/deintercalation, which thus increase the electrochemically active surface area of electrode as well as enhance the insertion/extraction kinetics.

To further study the mechanism of  $\text{FeF}_3 \cdot 0.33\text{H}_2\text{O}$  upon sodiation/desodiation, ex-situ XRD is used to observe the phase transformation and structure changes of the cycled AF-4 electrodes at different cycling stages. The electrodes (AF-0 and AF-4) that were not subjected to the charge/discharge cycle were named the Pre-cycled. (AF-0) and Pre-cycled. (AF-4). In Fig. 7a, three diffraction peaks marked with gray dotted line belong to that of the aluminum current collector. During the discharging process, the intensity of typical  $\text{FeF}_3 \cdot 0.33\text{H}_2\text{O}$  diffraction peaks gradually diminishes with the Na insertion proceeding and with a shift towards lower  $2\theta$  angles upon discharging to 2 V and 1.2 V, suggesting that a solid-solution behavior has generated due to the  $\text{Na}^+$  insertion into large-size tunnels based on Eq. (1) [48,57]. The decreased intensity of peaks is presumably associated to the stress and disorder because of the  $\text{Na}^+$  intercalation into  $\text{FeF}_3 \cdot 0.33\text{H}_2\text{O}$  cavities [33]. During the recharging process, the diffraction peaks centered at  $23.62^\circ$  and  $27.80^\circ$  can be obviously observed, implying the re-formation of  $\text{FeF}_3 \cdot 0.33\text{H}_2\text{O}$ . Consequently, the XRD patterns of  $\text{FeF}_3 \cdot 0.33\text{H}_2\text{O}$  collected for AF-4 are almost the same as the pre-cycled sample when recharged to 4.0 V, suggesting the high reversibility of AF-4 during the Na ion intercalation/deintercalation process as shown Eq. (1). However, the intensities of the peaks originated from  $\text{FeF}_3 \cdot 0.33\text{H}_2\text{O}$  in AF-0 is much weaker than that of AF-4 at 4.0 V due to the inadequate desodiation of the soliation products. The irreversibility of pure

$\text{FeF}_3 \cdot 0.33\text{H}_2\text{O}$  can be attributed to the structural change of the soliation/desodiation reaction. Above discussion of ex-XRD patterns for AF-4 and AF-0 during the charge/discharge process disclose that the appropriate  $\text{AlPO}_4$  modification is beneficial for alleviating the crystal structure change of  $\text{FeF}_3 \cdot 0.33\text{H}_2\text{O}$  and further enhance the cycling stability.

To determine the valence state of iron during the charge-discharge process, the ex-situ XPS of the cycled AF-4 electrodes at different cycling stages was tested, and the results were shown in Fig. 7b. During the discharging process, the Fe 2p XPS peaks of the AF-4 electrode shift to lower binding energy positions due to the reduction reaction of  $\text{Fe}^{3+}$  actuated by Na. Comparing to the pre-cycled sample, all satellite peaks of  $\text{Fe}^{3+}$  almost disappeared and the intensities of  $\text{Fe}^{2+}$  binding energy peaks increase, revealing the  $\text{Fe}^{3+}$  reducing to  $\text{Fe}^{2+}$ . When the AF-4 electrode further discharged to 1.2 V, binding energy peaks of Fe 2p<sub>3/2</sub> and Fe 2p<sub>1/2</sub> further shift to lower binding energy positions, which are in accordance with ex-situ XRD results. During the following charge process for 4.0 V, a reversed tendency of the shift in the XPS spectra is observed and the intensities of all peaks are similar to the pre-cycled sample, which reveals the oxidation of  $\text{Fe}^{2+}$  upon the extraction of  $\text{Na}^+$ . Above results indicate that AF-4 has good reversibility during the Na ion intercalation/deintercalation process. Moreover, the SEM images of AF-4 electrodes before cycling and after cycling were shown in Fig. 7a and b, respectively. SEM images of AF-4 electrode before the cycling show the spherical morphology, and it still maintains the similar morphology after 80 cycles, thus the morphology and structure of AF-4 sample keep excellent stability due to the existence of the appropriate amount of  $\text{AlPO}_4$  coating.

#### 4. Conclusions

The hollow porous  $\text{FeF}_3 \cdot 0.33\text{H}_2\text{O}$  microspheres have been successfully prepared via a solvothermal way through self-assembly as well as further modified with various amounts of  $\text{AlPO}_4$ . The unique hollow  $\text{FeF}_3 \cdot 0.33\text{H}_2\text{O}$  microspherical structures can shorten the path of  $\text{Na}^+$  diffusion and buffer the volume changes during cycling processes. Besides, with the appropriate amount of multifunctional  $\text{AlPO}_4$  coating layer, the charge transfer resistance of cell was decreased greatly and the  $\text{Na}^+$  diffusion coefficient was accelerated obviously. Compared to

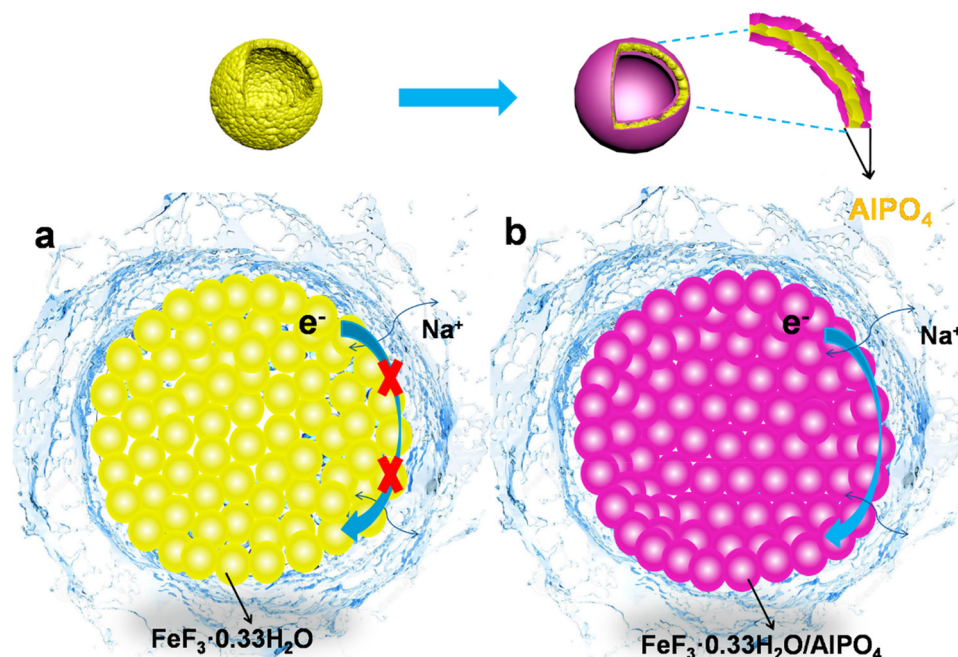


**Fig. 6.** Schematic illustration of reaction mechanism of (a) the pristine and (b)  $\text{AlPO}_4$ -coated  $\text{FeF}_3 \cdot 0.33\text{H}_2\text{O}$  cathodes.

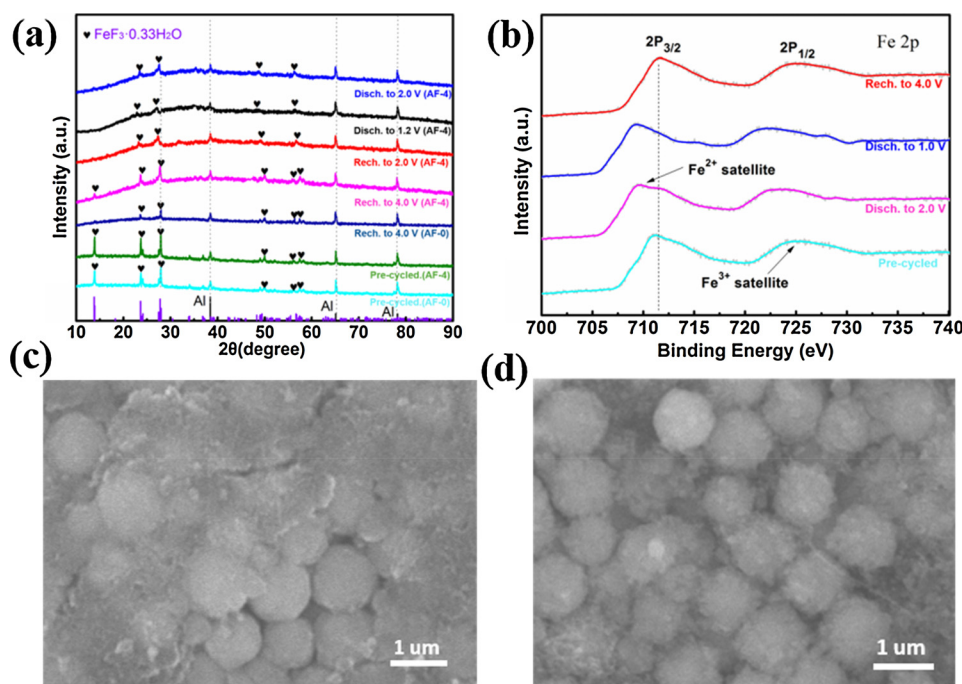


Fig. 7. (a) Ex-situ XRD patterns of AF-0 and AF-4 samples at different reaction stages of the first cycle. (b) The ex-situ XPS of the cycled AF-4 electrodes at different cycling stages. The SEM images of AF-4 electrode (c) before cycling and (d) after cycling.

the pristine  $\text{FeF}_3 \cdot 0.33\text{H}_2\text{O}$  (AF-0), 4 wt.%  $\text{AlPO}_4$ -coated  $\text{FeF}_3 \cdot 0.33\text{H}_2\text{O}$  (AF-4) exhibits a prominent initial discharge capacity of  $290 \text{ mAh g}^{-1}$ , outstanding cycle stability and excellent rate performance ( $167 \text{ mAh g}^{-1}$  at 2.0C). The excellent electrochemical performances are ascribed to the prominent “e-bridge” constructed by the appropriate  $\text{AlPO}_4$ -modification, enhancing electronic conductivity, reducing the side reaction between the electrode and electrolyte as well as unobstructed  $\text{Na}^+$  diffusion, which thus enhances the rate and cycling performances. Therefore, this work provides a significant exploration for designing and modifying low conductivity iron-based fluorides to apply as high-performance cathode materials of NIBs.

### Acknowledgements

This work is supported financially by the National Natural Science Foundation of China under project No. 51272221, Key Project of Strategic New Industry of Hunan Province under project No. 2016GK4005 and 2016GK4030.

### References

- [1] H. Kim, H. Kim, Z. Ding, M.H. Lee, K. Lim, G. Yoon, K. Kang, *Adv. Energy Mater.* 6 (2016) 1600943.
- [2] D. Kundu, E. Talaie, V. Duffort, L.F. Nazar, *Angew. Chem. Int. Ed.* 54 (2015) 3431–3448.
- [3] S.P. Ong, V.L. Chevrier, G. Hautier, A. Jain, C. Moore, S. Kim, X. Ma, G. Ceder, *Energy Environ. Sci.* 4 (2011) 3680–3688.
- [4] Z. Dai, U. Mani, H.T. Tan, Q. Yan, *Small Methods* 1 (2017) 1700098.
- [5] C. Fang, Y. Huang, W. Zhang, J. Han, Z. Deng, Y. Cao, H. Yang, *Adv. Energy Mater.* 6 (2016) 1501727.
- [6] M.H. Han, E. Gonzalo, G. Singh, T. Rojo, *Energy Environ. Sci.* 8 (2015) 81–102.
- [7] X. Xiang, K. Zhang, J. Chen, *Adv. Mater.* 27 (2015) 5343–5364.
- [8] Q. Ni, Y. Bai, F. Wu, C. Wu, *Adv. Sci.* 4 (2017) 1600275.
- [9] F. Wu, C. Wu, *Chin. Sci. Bull.* 59 (2014) 3369–3376.
- [10] I.D. Gocheva, M. Nishijima, T. Doi, S. Okada, J. Yamaki, T. Nishida, *J. Power Sources* 187 (2009) 247–252.
- [11] Y. Xu, Q. Wei, C. Xu, Q. Li, Q. An, P. Zhang, J. Sheng, L. Zhou, L. Mai, *Adv. Energy Mater.* 6 (2016) 1600389.
- [12] Y. Dong, S. Li, K. Zhao, C. Han, W. Chen, B. Wang, L. Wang, B. Xu, Q. Wei, L. Zhang, X. Xu, L. Mai, *Energy Environ. Sci.* 8 (2015) 1267–1275.
- [13] Y. Han, J. Hu, C. Yin, Y. Zhang, J. Xie, D. Yin, C. Li, *J. Mater. Chem. A* 4 (2016) 7382–7389.
- [14] F. Wu, G. Yushin, *Energy Environ. Sci.* 10 (2017) 435–459.
- [15] M. Nishijima, I.D. Ocheva, S. Okada, T. Doi, J. Yamaki, T. Nishida, *J. Power Sources* 190 (2009) 558–562.
- [16] C. Li, C. Yin, L. Gu, R.E. Dinnebier, X. Mu, P.A. van Aken, J. Maier, *J. Am. Chem. Soc.* 135 (2013) 11425–11428.
- [17] J. Yang, Z. Xu, H. Zhou, J. Tang, H. Sun, J. Ding, X. Zhou, *J. Power Sources* 363 (2017) 244–250.
- [18] C. Li, C. Yin, X. Mu, J. Maier, *Chem. Mater.* 25 (2013) 962–969.
- [19] F. Badway, N. Pereira, F. Cosandey, G.G. Amatucci, *J. Electrochem. Soc.* 150 (2003) A1209–A1218.
- [20] Y.K. Kim, J.K. Lee, J. Kim, *Bull. Korean Chem. Soc.* 36 (2015) 1878–1884.
- [21] Y. Bai, X. Zhou, C. Zhan, L. Ma, Y. Yuan, C. Wu, M. Chen, G. Chen, Q. Ni, F. Wu, R. Shahbazian-Yassar, T. Wu, J. Lu, K. Amine, *Nano Energy* 32 (2017) 10–18.
- [22] J. Tan, L. Liu, H. Hu, Z. Yang, H. Guo, Q. Wei, X. Yi, Z. Yan, Q. Zhou, Z. Huang, H. Shu, X. Yang, X. Wang, *J. Power Sources* 251 (2014) 75–84.
- [23] L.S. Li, F. Meng, S. Jin, *Nano Lett.* 12 (2012) 6030–6037.
- [24] Y. Lu, Z.Y. Wen, K. Rui, X.W. Wu, *J. Power Sources* 24 (2013) 306–311.
- [25] Y. Lu, Z.Y. Wen, J. Jin, K. Rui, *Phys. Chem. Chem. Phys.* 16 (2014) 8556–8562.
- [26] B.J. Li, Z.J. Cheng, N.Q. Zhang, K.N. Sun, *Nano Energy* 4 (2014) 7–13.
- [27] Q.X. Chu, Z.C. Xing, J.Q. Tian, X.B. Ren, *J. Power Sources* 236 (2013) 188–191.
- [28] J. Liu, W. Liu, S.M. Ji, Y.L. Wan, *Chem. Eur. J.* 20 (2014) 5815–5820.
- [29] L. Liu, M. Zhou, L. Yi, H. Guo, J. Tan, H. Shu, X. Yang, Z. Yang, X. Wang, *J. Mater. Chem.* 22 (2012) 17539–17550.
- [30] M. Liu, X. Wang, S. Wei, H. Hu, R. Zhang, L. Liu, *Electrochim. Acta* 269 (2018) 479–489.
- [31] Y. Bai, X.Z. Zhou, J. C. Wu, L. Yang, M. Chen, H. Zhao, F. Wu, G. Liu, *Nano Energy* 17 (2015) 140–151.
- [32] G. Ali, S.H. Oh, S.Y. Kim, J.Y. Kim, B.W. Cho, K.Y. Chung, *J. Mater. Chem. A* 3 (2015) 10258–10266.
- [33] G. Ali, J.H. Lee, B.W. Cho, K.-W. Nam, D. Ahn, W. Chang, S.H. Oh, K.Y. Chung, *Electrochim. Acta* 191 (2016) 307–316.
- [34] C. Li, L. Gu, J. Tong, J. Maier, *ACS Nano* 5 (2011) 2930–2938.
- [35] Y. Shen, X. Wang, H. Hu, M. Jiang, X. Yang, H. Shu, *J. Power Sources* 283 (2015) 204–210.
- [36] M. Jiang, X. Wang, H. Hu, Y. Fu, S. Wei, Y. Shen, *J. Power Sources* 316 (2016) 170–175.
- [37] M. Jiang, X. Wang, S. Wei, Y. Shen, H. Hu, *J. Alloys. Compd.* 670 (2016) 362–368.
- [38] R.S. Rao, V. Pralong, U.V. Varadaraju, *Solid State Sci.* 55 (2016) 77–82.
- [39] Y. Li, X. Zhou, Y. Bai, G. Chen, Z. Wang, H. Li, F. Wu, C. Wu, *ACS Appl. Mater. Interfaces* 9 (2017) 19852–19860.
- [40] W. Wu, X.Y. Wang, X. Wang, S.Y. Yang, *Mater. Lett.* 63 (2009) 1788–1790.
- [41] W. Wu, Y. Wang, X.Y. Wang, Q.Q. Chen, *J. Alloys. Compd.* 486 (2009) 93–96.
- [42] R. Zhang, X. Wang, S. Wei, X. Wang, M. Liu, H. Hu, *J. Alloys. Compd.* 719 (2017) 331–340.
- [43] J. Cho, Y.W. Kim, B. Kim, J.G. Lee, B. Park, *Angew. Chem. Int. Ed.* 42 (2003) 1618–1621.
- [44] F. Wu, X. Zhang, T. Zhao, L. Li, M. Xie, R. Chen, *ACS Appl. Mater. Interfaces* 7 (2015) 3773–3781.
- [45] J.-H. Lee, S.-H. Lee, *ACS Appl. Mater. Interfaces* 8 (2016) 28974–28981.
- [46] B. Hu, X. Wang, Y. Wang, Q. Wei, Y. Song, H. Shu, X. Yang, *J. Power Sources* 218

- (2012) 204–211.
- [47] A.T. Appapillai, A.N. Mansour, J. Cho, Y. Shao-Horn, *Chem. Mater.* 19 (2007) 5748–5757.
- [48] C. Li, L. Gu, J. Tong, S. Tsukimoto, J. Maier, *Adv. Funct. Mater.* 21 (2011) 1391–1397.
- [49] W. An, J. Fu, J. Su, L. Wang, X. Peng, K. Wu, Q. Chen, Y. Bi, B. Gao, X. Zhang, *J. Power Sources* 345 (2017) 227–236.
- [50] W. An, J. Fu, S. Mei, L. Xia, H. Gu, X. Zhang, B. Gao, X. Li, P.K. Chu, K. Huo, *J. Mater. Chem. A* 5 (2017) 14422–14429.
- [51] X. Li, Y. Zhang, Y. Meng, G. Tan, J. Ou, Y. Wang, Q. Zhao, H. Yuan, D. Xiao, *Chem. Electro. Chem.* 4 (2017) 1–8.
- [52] M. Jiang, X. Wang, Y. Shen, H. Hu, Y. Fu, X. Yang, *Electrochim. Acta* 186 (2015) 7–15.
- [53] G.-R. Hu, X.-R. Deng, Z.-D. Peng, K. Du, *Electrochim. Acta* 53 (2008) 2567–2573.
- [54] K.S. Tan, M.V. Reddy, G.V.S. Rao, B.V.R. Chowdari, *J. Power Sources* 141 (2005) 129–142.
- [55] Z. Li, B. Wang, C. Li, J. Liu, W. Zhang, *J. Mater. Chem. A* 3 (2015) 16222–16228.
- [56] S.Y. Wei, X.Y. Wang, M.L. Jiang, R. Zhang, Y.Q. Shen, H. Hu, *J. Alloys Compd.* 689 (2016) (2016) 945–951.
- [57] L. Li, R. Jacobs, P. Gao, L. Gan, F. Wang, D. Morgan, S. Jin, *J. Am. Chem. Soc.* 138 (2016) 2838–2848.
- [58] F. Gao, Z. Tang, *Electrochim. Acta* 53 (2008) 5071–5075.